ORIGINAL PAPER

From Ultraslow to Extremely Fast Dynamics in Sodium Nitrate: an ^{17}O NMR Study

J. Beerwerth[1] ⬤ **· R. Siegel[2] · L. Hoffmann[1]** ⬤ **· L. S. Plaga[1] · M. Storek[1] · B. Bojer[2] · J. Senker[2] · W. Hiller[3] · R. Böhmer[1]** ⬤

Abstract

Increasing dynamics in solids featuring nuclei subjected to second-order quadrupolar interactions lead to central-transition spectra that undergo two consecutive line-shaped transitions. Conventional motional narrowing occurs when the molecular exchange rate is on the order of the strength of the dominant interaction. In a second step, the resulting intermediately narrowed spectra change further when the motion becomes faster than the Larmor precession rate, leading to terminally narrowed spectra that can display a residual quadrupolar shift. We derive analytic expressions for this shift and analyze the quadrupolar central-transition spectra in terms of C_N symmetrical cone models. Increasing the number of sites to $N \geq 3$, the terminally narrowed spectra remain unaltered, while the intermediately narrowed spectra remain unaltered only for $N \geq 5$. This finding relates to the different (cubic vs. icosahedral) symmetries that are required to average out the spatial second- and fourth-rank terms in the second-order quadrupolar interaction. Following recent work (Hung et al., Solid State Nucl Magn Reson 84:14–19, 2017), ^{17}O NMR is applied to examine the three-site rotation of the nitrate group in $NaNO_3$. Line shapes are measured and analyzed, and in addition to prior work, satellite-transition and stimulated-echo experiments are carried out. The final-state amplitudes extracted from the latter are reproduced using model calculations. It is shown how two-dimensional exchange spectra relating to N-site cone motions can be decomposed in terms of effective two-site-jump spectra. This latter approach is successfully tested for $NaNO_3$.

✉ J. Beerwerth
  joachim.beerwerth@tu-dortmund.de

[1] Fakultät Physik, Technische Universität Dortmund, 44221 Dortmund, Germany

[2] Anorganische Chemie III, Universität Bayreuth, 95440 Bayreuth, Germany

[3] Fakultät für Chemie und Chemische Biologie, Technische Universität Dortmund, 44221 Dortmund, Germany

1 Introduction

For many nuclear magnetic resonance (NMR) studies, observing motion-induced spectral narrowing is an indispensable source of information to map out the molecular dynamics in solid- and liquid-like materials [1]. Tracing the dynamics of such materials using, e.g., popular spin-1/2 probes, the motional narrowing observed when increasing the sample temperature is typically found complete if the molecular reorientation rates exceed the spectral width accessible via the probe nucleus. For isotropic molecular motions, motional narrowing effects usually lead to narrow, "fully averaged" spectra. Conversely, if the molecular motion is anisotropic, a significant residual line width usually remains. In the presence of first-order anisotropies originating, e.g., from chemical shift or relatively small quadrupolar interactions, many scenarios of molecular motions and their impact on the resulting high-temperature NMR spectra were considered [2–4].

Currently, also the exploitation of nuclear probes with spins $I > 1$ is of particular interest when studying molecular or ionic dynamics since many applications in the life and materials sciences require alkali, oxygen, and many other nuclear probes with half-integer spin $I > 1$ [5–10].

Recently, it was emphasized that in the presence of second-order quadrupolar interactions, an interesting motional narrowing scenario can arise. In their ^{17}O NMR study on $NaNO_3$, Hung et al. [11] pointed out that "for central-transition spectra of half-integer quadrupolar nuclei in solids, line shape change due to molecular dynamics occurs in two stages. The first stage occurs when the exchange rate is comparable to the second-order quadrupolar interaction. The second spectral transition comes at a faster exchange rate which approaches the Larmor frequency and generally reduces the isotropic quadrupolar shift". In other words, for strongly quadrupolarly perturbed nuclei, an intermediate motional narrowing (IMN) precedes what may be called terminal motional narrowing (TMN). In that latter regime, the spectra can still exhibit a significant, non-Lorentzian line shape. A quantitative description of the spectra referring to the transition between the two narrowing regimes usually requires numerical calculations in terms of the stochastic Liouville equation [12, 13].

By contrast, in the presence of *isotropic* motions, a simpler description is possible for strongly perturbed quadrupolar probes [14–16]. Here, the transition between the two narrowing regimes usually involves a description in terms of a multiexponential dephasing and leads from one Lorentzian line to another Lorentzian line when progressing from (conventional) motional narrowing to extreme narrowing. The interesting effects of second-order quadrupolar broadening [17] and second-order quadrupolar shift [18] which occur between the two corresponding dynamical ranges were recently exploited in studies of glass forming materials not only using the ^{17}O probe but also employing other nuclei such as ^{11}B and ^{87}Rb [19–21].

Spectra in the TMN regime, with *anisotropic* motions fast on the Larmor scale, can often be assessed analytically in terms of an orientational averaging carried out over the sites visited during the motion. In the literature, examples for

such an averaging are discussed in relation to (relatively small) first-order anisotropies, see e.g., [3] and references cited therein. Here, we will elucidate the consequences of such an averaging also in view of (much larger) second-order anisotropies. Furthermore, the only partial quenching of the isotropic (low-temperature) second-order quadrupolar shift by rapid, but anisotropic reorientational motions is also explored. These results, mostly obtained in the framework of discrete N-site cone models featuring C_N symmetry, should be useful to describe the regime of fast molecular motions in crystalline samples. There are various examples from ^{17}O NMR for crystalline materials that owing to their structure can display twofold [22–24], threefold [25–27], fourfold [10], or sixfold [28, 29] molecular jump processes.

On the experimental side, we examine oxygen-17 labeled $NaNO_3$ in a temperature range that is somewhat larger than covered previously [11]. Thus, at the highest temperature, where a truncation of the second-order Hamiltonian is not permissible, we study not only the central-transition but the satellite lines as well. On the low-temperature side, where the average Hamiltonian approximation can be applied, central-transition stimulated-echo experiments are performed to map out motional time scales. Using this method, we obtain correlation times at temperatures which are significantly lower than those previously accessed [11]. We compare these time constants with prior results and with results obtained using spin–lattice relaxometry. Based on evolution-time-dependent stimulated-echo experiments, final-state amplitudes are determined and compared with numerical simulations. Furthermore, in the spirit of former approaches [30], we show how two-dimensional exchange spectra relating to N-site cone motions can be represented as a properly weighted sum of effective two-site jumps.

2 Theoretical Considerations

2.1 Motional Averaging of Nonsecular Hamiltonians

In this section, we will outline the framework important to distinguish the various modes of motional and orientational averaging, e.g., to be able to calculate residual second-order quadrupolar shifts and couplings in the TMN regime. In the principal axis system (PAS) of the electrical field gradient (EFG) tensor with its Cartesian components $|V_{ZZ}| \geq |V_{YY}| \geq |V_{XX}|$, the quadrupolar interaction can be described by the Hamiltonian [31, 32]

$$H_Q = \frac{e^2qQ}{2I(2I-1)\hbar} \frac{1}{2} \left\{ 3I_z^2 - I(I+1) + \frac{1}{2}\eta Q(I_x^2 - I_y^2) \right\}. \tag{1}$$

Since the EFG tensor is traceless, in its PAS, it suffices to describe it using two parameters. To this end, often the quadrupolar coupling constant $C_Q = e^2qQ/h$ (in Hertz, or the largest tensor component, $V_{ZZ} = eq$) and the asymmetry parameter $\eta_Q = (V_{XX} - V_{YY})/V_{ZZ}$ are chosen.

Overall, the Hamiltonian may contain other contributions such as arising from the Zeeman or the chemical shift interaction, so that in the laboratory frame (LAB), one has

$$H_{\text{LAB}} = H_{\text{Z}} + H_{\text{Q,LAB}} + H_{\text{CS,LAB}}. \tag{2}$$

The succession of coordinate transformations leading from the PAS of the corresponding chemical shift or quadrupolar tensors (abbreviated as 'CS' and 'Q') via the crystal-fixed system (CFS) to the LAB can symbolically be written as

$$\text{CS} \xrightarrow{\Omega_1} \text{Q} \xrightarrow{\Omega_2} \text{CFS} \xrightarrow{\Omega_3} \text{LAB}. \tag{3}$$

Here, Ω represents the set of Euler angles that is needed to accomplish each transformation, for example

$$\Omega_2 = \Omega_{\text{Q}\to\text{CFS}} = \left\{ \alpha_{\text{Q}\to\text{CFS}}, \beta_{\text{Q}\to\text{CFS}}, \gamma_{\text{Q}\to\text{CFS}} \right\}. \tag{4}$$

To implement the associated rotations elegantly, a representation of the Hamiltonian in terms of the spherical tensor components T_{lm} and V_{lm} is useful. Usually, one starts from the secular Hamiltonian which for the quadrupolar interaction reads

$$H_{\text{Q, LAB}} = \frac{eQ}{2I(2I-1)\hbar} \sum_{m=-2}^{2} (-1)^m V_{2,-m}^{\text{Q,LAB}} T_{2,m}^{\text{Q}}. \tag{5}$$

Here, l and m designate the rank and order of the tensor components, respectively. For the spatial components

$$V_{2,m}^{\text{Q,LAB}} = \sum_{k=-2}^{2} \sum_{n=-2}^{2} D_{k,m}^{(2)}(\Omega_3) D_{n,k}^{(2)}(\Omega_2) V_{2,n}^{\text{Q,PAS}} \tag{6a}$$

$$= \sum_{k=-2}^{2} D_{k,m}^{(2)}(\Omega_3) V_{2,k}^{\text{Q,CFS}}, \tag{6b}$$

the succession of transformations from the PAS to the LAB is achieved by means of the second-rank Wigner rotation matrix elements $D_{i,m}^{(2)}(\Omega)$. In Eq. (6b), the transformation is written to start from the CFS. Various definitions are in use for the spatial components in the PAS; here, we employ [32]

$$V_{2,0}^{\text{Q,PAS}} = \sqrt{\frac{3}{2}}eq, \quad V_{2,\pm1}^{\text{Q,PAS}} = 0, \quad V_{2,\pm2}^{\text{Q,PAS}} = \frac{1}{2}eq\eta. \tag{7}$$

In view of some of the experimental results that will be reported below, we will now assume that the molecular motion is fast on the time scale set by $1/\omega_{\text{L}}$. For such extremely fast motions, rather than applying Eq. (6), it is advisable to perform first an averaging over the molecular motion which is conveniently possible in the CFS. We will further assume that in the crystal, the molecule (more precisely: the orientation of the largest principal axis of the corresponding EFG

tensor) can hop among N sites described by $\Omega_{2,s} = \{\alpha_s, \beta_s, \gamma_s\}$ where the sites are numbered by $s = 1, \ldots, N$. In this coordinate frame, the motionally averaged tensor components are

$$\overline{V}_{2,k}^{\text{Q,CFS}} = \sum_{s=1}^{N} V_{2,k}^{\text{Q,CFS},s} = \sum_{n=-2}^{2} V_{2,n}^{\text{Q,PAS},s} \frac{1}{N} \sum_{s=1}^{N} D_{n,k}^{(2)}(\Omega_2) \tag{8}$$

which yields the lab frame tensor components

$$\overline{V}_{2,m}^{\text{Q,LAB}} = \sum_{k=-2}^{2} D_{k,m}^{(2)}(\Omega_3) \overline{V}_{2,k}^{\text{Q,CFS}}. \tag{9}$$

Hence, the quadrupolar Hamiltonian now reads

$$\overline{H}_{\text{Q,LAB}} = \frac{eQ}{2I(2I-1)\hbar} \sum_{m=-2}^{2} (-1)^m \overline{V}_{2,-m}^{\text{Q,LAB}} T_{2,m}^{\text{Q}}. \tag{10}$$

To derive the relevant NMR frequencies, one usually starts from the interaction representation and performs the secular approximation. Note that here we do not start from Eq. (5), which would be suitable for molecular motions slow on the ω_{L} scale, but from Eq. (10) instead. In other words, now the motionally averaged tensor components are 'slow' on this scale; in fact, in the CFS, they are constant.

Transforming $\overline{H}_{\text{Q,LAB}}$ to the rotating frame and averaging over one Larmor period $t_{\text{L}} = 2\pi/\omega_{\text{L}}$, in Eq. (10), the terms with $m \neq 0$ vanish, thus yielding the first-order quadrupolar Hamiltonian

$$\begin{aligned}\overline{H}_{\text{Q,LAB}}^{(1)} &= \frac{eQ}{2I(2I-1)\hbar} \overline{V}_{2,0}^{\text{Q,LAB}} \frac{1}{\sqrt{6}} \{3I_z^2 - I(I+1)\} \\ &= \frac{eQ}{2I(2I-1)\hbar} \overline{V}_{2,0}^{\text{Q,LAB}} T_{2,0}^{\text{Q}}.\end{aligned} \tag{11}$$

For convenience, the Hamiltonian in Eq. (11) is written in terms of spherical as well as of Cartesian operators. This leads to the *orientationally* averaged (not to be confused with the powder averaged) NMR frequencies

$$\overline{\omega}_{m-1,m}^{(1)} = \langle m-1|\overline{H}_Q^{(1)}|m-1\rangle - \langle m|\overline{H}_Q^{(1)}|m\rangle. \tag{12}$$

In the fast-motion regime, with motional rates larger than about C_Q, one thus has

$$\overline{\omega}_{m-1,m}^{(1)} = \overline{\overline{\omega}_{m-1,m}^{(1)}} = \frac{3}{\sqrt{6}} \frac{eQ}{2I(2I-1)\hbar} (1-2m) \overline{V}_{2,0}^{\text{Q,LAB}}, \tag{13}$$

where the large overbar reflects *motional* averaging, rather than the orientational averaging discussed above. In other words, there is no line shape change when going from the fast-motion to the extreme-narrowing regime. This statement applies in

particular also to the CS anisotropy which, therefore, does not require separate treatment. For convenience, for this interaction, the presently employed nomenclature is outlined in the "Appendix".

Now, applying the secular approximation to Eq. (10) also for the terms with $m \neq 0$, one obtains

$$
\begin{aligned}
\bar{H}^{(2)}_{\text{Q,LAB}} = {} & \frac{1}{2\omega_{\text{L}}} \left(\frac{eQ}{2I(2I-1)\hbar} \right) \\
& \times \Big\{ \bar{V}^{\text{Q,LAB}}_{2,-2} \bar{V}^{\text{Q,LAB}}_{2,2} \big([2I(I+1) - 1]I_z - 2I_z^3 \big) \\
& + \bar{V}^{\text{Q,LAB}}_{2,-1} \bar{V}^{\text{Q,LAB}}_{2,1} \big([4I(I+1) - 1]I_z - 8I_z^3 \big) \Big\}.
\end{aligned}
\tag{14}
$$

Let us re-iterate that this Hamiltonian has been obtained by first performing motional averaging and then applying the secular approximation. Thus, Eq. (14) can be exploited to analyze dynamics faster than ω_{L}, while $H_Q^{(2)}$ (without overbar) is applicable only if molecular motion much slower than ω_{L} is considered. Note that for the second-order frequency

$$
\overline{\omega}^{(2)}_{m-1,m} = \langle m-1 | \overline{H}_Q^{(2)} | m-1 \rangle - \langle m | \overline{H}_Q^{(2)} | m \rangle,
\tag{15}
$$

generally, we have $\overline{\omega}^{(2)}_{m-1,m} \neq \overline{\omega^{(2)}_{m-1,m}}$ which gives rise to a "second spectral transition" [11].

For isotropic motions (or if the underlying process exhibits at least icosahedral symmetry), the products of the spatial tensor components appearing in Eq. (14) vanish. However, for anisotropic motions in general, a residual quadrupolar-induced isotropic shift will remain.

To determine this shift, it is convenient to decompose the products $\bar{V}^{\text{Q,LAB}}_{2,-m} \bar{V}^{\text{Q,LAB}}_{2,m}$ in terms of the spatial tensor elements $W_{l,0}$ with rank $l = 0$, 2, and 4. By virtue of the Clebsch–Gordan coefficients, one may write [33]

$$
V_{2,-1} V_{2,1} = \sqrt{\frac{8}{35}} W_{4,0} + \frac{1}{\sqrt{14}} W_{2,0} - \frac{1}{\sqrt{5}} W_{0,0},
\tag{16a}
$$

and

$$
V_{2,-2} V_{2,2} = \frac{1}{\sqrt{70}} W_{4,0} + \sqrt{\frac{2}{7}} W_{2,0} + \frac{1}{\sqrt{5}} W_{0,0}.
\tag{16b}
$$

In this 'coupled' representation, the isotropic (i.e., orientation independent, thus frame invariant) component is [33]

$$
W_{0,0} = W^{\text{PAS}}_{0,0} = \frac{2(V^{\text{PAS}}_{2,2})^2 + (V^{\text{PAS}}_{2,0})^2}{\sqrt{5}} = \frac{\sqrt{5}}{10} (eq)^2 (\eta^2 + 3),
\tag{17}
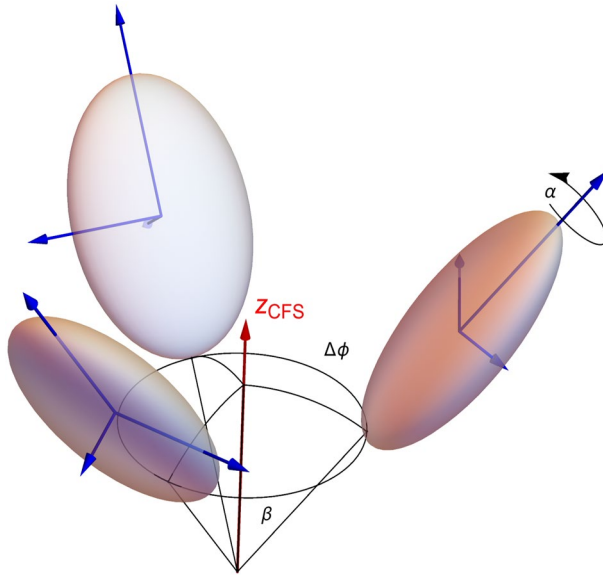$$

if a motional pre-averaging is *not* applied.

Fig. 1 Illustration of a three-site cone model where the cone exhibits a half opening angle β. The difference of the azimuthal angles of two adjacent sites is $\Delta\phi$, e.g., $|\gamma_1 - \gamma_2|$. For illustration purposes the largest principal axes of the EFG tensors (here with $\eta = 0.4$) are chosen to lie along the cone mantle and the second-largest axes are tangential to its circumference (corresponding to an angle $\alpha = 0°$). The symmetry axis of the cone is chosen to coincide with the z-axis of the crystal-fixed coordinate system

In the regime of extreme motional narrowing, however, one should instead start from the *averaged* tensor elements $\overline{V}_{2,m}^{\mathrm{Q,CFS}}$. Now assessing the rank-zero term, we obtain

$$W_{0,0}^{\mathrm{Q}} = \frac{1}{\sqrt{5}}\left[2\overline{V}_{2,+2}^{\mathrm{Q,CFS}}\overline{V}_{2,-2}^{\mathrm{Q,CFS}} - 2\overline{V}_{2,+1}^{\mathrm{Q,CFS}}\overline{V}_{2,-1}^{\mathrm{Q,CFS}} + (\overline{V}_{2,0}^{\mathrm{Q,CFS}})^2\right]. \tag{18}$$

With the tensor components averaged in a proper PAS, the $\overline{V}_{2,\pm1}^{\mathrm{Q,CFS}}$ terms vanish and one has $\overline{V}_{2,+2}^{\mathrm{Q,CFS}} = \overline{V}_{2,-2}^{\mathrm{Q,CFS}}$ so that Eq. (17) results. Obviously, as will be exploited below, the averaged residual quadrupolar-induced shift will depend on the motional model.

2.2 Cone Models: Extreme Narrowing and Residual Shifts

Focusing first on the motionally averaged second-order quadrupolar Hamiltonian $\overline{H}_{\mathrm{Q}}^{(2)}$ when calculating the NMR spectra in the extreme narrowing limit, the decisive step is to evaluate Eq. (8). Here, it is written more explicitly as

$$\overline{V}_{2,q}^{\mathrm{Q,CFS}} = (-1)^q \sum_{q'=-2}^{2} V_{2,q'}^{\mathrm{Q,PAS}} e^{-iq'\alpha} d_{q',q}^{(2)}(\beta) \frac{1}{N}\sum_{s=1}^{N} f_i e^{iq\gamma_s}, \tag{19}$$

where the population f_i for site i with $\Sigma_i f_i = 1$ as well as the reduced Wigner matrix elements $d^{(2)}_{q',q}(\beta)$ are introduced. Note that the first rotation in the motionless CFS is about the z_{CFS}-axis by an angle α, the β rotation about the y_{CFS}-axis, and the last rotation about the z_{CFS}-axis by the azimuthal angle γ_s [34]. Thus, for $\eta = 0$, the angle α is irrelevant. Figure 1 illustrates these rotations for a molecular jump among $N = 3$ equivalent sites.

In Eq. (19), the sum over the N discrete sites can be generalized to continuous distributions of angles, $\langle e^{iq\gamma} \rangle$, with Ref. [3] listing a number of relevant cases for such averages. The determination of averaged tensors is independent of the form of the Hamiltonian. Thus, the same averaging of the anisotropy and asymmetry parameters applies for which examples with respect to various jump models were given previously [2–4]. In particular, under conditions of extreme narrowing, the averaged EFG tensor parameters are simply obtained by diagonalizing the averaged tensor.

This implies that for $N \geq 3$ equivalent sites an averaged asymmetry parameter $\overline{\eta} = 0$ results [4] and an averaged quadrupolar coupling constant $\overline{C}_Q$ that can be used to define a quadrupolar narrowing factor

$$N_Q = \overline{C}_Q/C_Q = \tfrac{1}{2}\left(3\cos^2\beta - 1 + \eta_Q \sin^2\beta\cos 2\alpha\right). \tag{20}$$

For NaNO$_3$ using $\alpha = 0°$, $\beta = 90°$, and $\eta_Q = 0.8$ [11], one finds $N_Q = \tfrac{1}{2}(-1 + \eta_Q) = -0.1$. This example shows that the narrowing factor can become negative, just like for the chemical shielding anisotropy for which an analogous factor $N_{CS} = \overline{\zeta}_{CS}/\zeta_{CS}$ can be defined. For NaNO$_3$ using $\beta = 180°$ [11], one finds that $N_{CS} = \tfrac{1}{2}(3 - 1 + 0\eta_{CS}) = 1$. However, unlike for the chemical shielding anisotropy, the sign of N_Q is not generally accessible from pure quadrupolar spectra because the first-order spectra are already symmetric and in second-order the *squared* coupling appears.

Likewise, for anisotropic motions a residual quadrupolar-induced shift remains in the fast-motion limit. This shift that we call δ_{QIS} depends on the type of motion. Assessing Eq. (17), we arrive at

$$
\begin{aligned}
\delta_{QIS} &= \frac{1}{\sqrt{5}}\frac{I(I+1) - 9(m+1)m - 3}{\omega_L^2}\left(\frac{eQ}{2I(2I-1)\hbar}\right)^2 W^Q_{0,0}\\
&= \frac{I(I+1) - 9(m+1)m - 3}{30\omega_L^2}\left(\frac{3e^2qQ}{2I(2I-1)\hbar}\right)^2 N_Q^2\left(1 + \frac{\overline{\eta}^2}{3}\right).
\end{aligned}
\tag{21}
$$

It is also useful to express the residual quadrupolar-induced shift of the central line, $\overline{v}^{(Q)}_{CG}$, in frequency units. Together with[1] $\overline{v}^{exp}_{CG} = v^{(CS)}_{iso} + \overline{v}^{(Q)}_{CG}$, where $v^{(CS)}_{iso}$ refers to the (usual) isotropic chemical shift, the experimentally observed center-of-gravity frequency is

---

[1] For the corresponding expressions in Refs. [20, 21] the minus signs should be replaced by plus signs.

$$\overline{v}_{CG}^{exp} = v_{iso}^{(CS)} \underbrace{- \frac{3}{40} \frac{I(I+1) - \frac{3}{4}}{[I(2I-1)]^2}}_{=-3/500 \text{ for } I=5/2} \frac{\overline{C}_Q^2}{v_L} \left(1 + \frac{1}{3}\overline{\eta}_Q^2\right). \tag{22}$$

cf. Refs. [16, 35]. For $N=2$, the quantities $\overline{C}_Q$ and $\overline{\eta}_Q$ have to be calculated as described, e.g., in Refs. [2, 4]. Interestingly, the *first-order*-like expression, Eq. (20), is to be used in conjunction with the angular dependence of the *second-order* quadrupolar frequencies.

2.3 Slow and Ultraslow Motions

To describe molecular motions that take place on time scales much longer than $1/\omega_L$, the Hamiltonian is obtained as usual, i.e., by applying the secular approximation *before* any motional averaging is performed. This leads to the quadrupolar Hamiltonian of the form of Eq. (14), but without overbars. In the frame rotating with ω_L, the resulting quadrupolar frequency is $\omega_{m-1,m} = \omega_{m-1,m}^{(1)} + \omega_{m-1,m}^{(2)}$. The first-order frequencies are given by Eq. (13) and the second-order frequencies can be written as [36]

$$\begin{aligned}
\omega_{m-1,m}^{(2)} = \frac{1}{2\omega_L} &\left(\frac{eQ}{2I(2I-1)\hbar}\right) \\
&\times \Big\{ V_{2,-2}^{Q,LAB} V_{2,2}^{Q,LAB}(6m(m-1) - 2I(I+1) + 6) \\
&+ V_{2,-1}^{Q,LAB} V_{2,1}^{Q,LAB}(24m(m-1) - 4I(I+1) + 9).
\end{aligned} \tag{23}$$

Practical expressions applicable for static and rotating samples are given elsewhere, e.g., in Ref. [32] and will not be reproduced here. Equation (23) in combination with random walk simulations [23, 37, 38] can be exploited to calculate central-transition and satellite-transition spectra. For motions slow on the scale set by $1/\omega_L$ and in the presence of a sufficiently large quadrupolar coupling, typically only the central transition can be excited. In the remainder of this section, we will, therefore, focus on $\omega_{-1/2,1/2}^{(2)} \equiv \omega_c$.

By exploiting the transformations from the PAS to the LAB, with the angles defined in $\Omega_{2,s} = \{\alpha_s, \beta_s, \gamma_s\}$ and $\Omega_{3,s} = \{\phi, \theta, 0\}$, it is always possible to analyze the underlying frequency distributions for motional processes taking place with rates Γ in the INM regime, $2\pi C_Q < \Gamma << \omega_L$. Schurko et al. [10] showed that and explained why in this regime it is not generally possible to describe the second-order central-transition spectra in terms of effective anisotropy and asymmetry parameters. Expressed in our terms, rather than assessing the products of the site averages, $\overline{V}_{2,-q}^{Q,LAB} \overline{V}_{2,q}^{Q,LAB}$, cf. Eq. (9), the site-averaged products $V_{2,-q}^{Q,LAB} V_{2,q}^{Q,LAB}$ need to be assessed. Following previous procedures [23], for an N-site jump model, it is, therefore, useful to evaluate the frequencies distribution

$$\overline{\omega_{c,N}}(\theta, \phi, \varphi, \eta) = \sum_{s=1}^{N} f_s\, \omega_{c,s}(\alpha_s, \beta_s, \gamma_s; \theta, \phi, \varphi, \eta). \tag{24}$$

Here, the frequencies $\omega_{c,s}$ are calculated according to Eq. (6), and the f_i coefficients still represent normalized population factors. The large overbar in Eq. (24) is again meant to refer to an averaging over all sites s that are accessed in the course of the molecular motion. The $N=2$ case, i.e., a jump among two sites has already been discussed [23]. Hence, here we will focus on cone models with $N \geq 3$. When assessing Eq. (24), it turns out[2] that for $N \geq 5$ sites the frequency distributions and consequently all quantities than can be derived thereof—like the corresponding NMR spectra—do not depend on the number of sites. For the second-order quadrupolar interaction with its rank $l=4$ terms, this finding is not entirely unexpected since it was stated that [39]: "the anisotropy described by tensor components $A_{lm\neq0}$ for a particular l can be averaged away by reorienting the sample so that the field is directed at $N=l+1$ or more directions to form a cone". The A_{lm} coefficients used in Ref. [39], in the present notation are related to the spatial tensor components $V_{2,-q}^{Q} V_{2,q}^{Q}$, cf. Eq. (16). In other words, first-order ($l=2$) anisotropies can be averaged out by motions on cones with $N=3$ equivalent sites, while for second-order ($l=4$) terms one needs five such sites.

This argument is also relevant in the ultraslow regime. Here, it is possible to map out molecular motions by generating time-domain signals of the form [40]

$$F_2^{\cos}(t_1, t_m, t_2) = \frac{3}{4I(I+1)} \cos\big(\omega_c(0)t_1\big) \cos\big(\omega_c(t_m)t_2\big) \tag{25a}$$

and

$$F_2^{\sin}(t_1, t_m, t_2) = \frac{3}{4I(I+1)} \sin\big(\omega_c(0)t_1\big) \sin\big(\omega_c(t_m)t_2\big) \tag{25b}$$

by applying three or more suitably phased radio-frequency pulses. The form in Eq. (25) arises if signal maximizing flip angles are assumed so that for $I=5/2$ spins, the prefactor appearing in Eq. (25) is 3/35.[3] The hypercomplex data set represented by Eq. (25) can be properly Fourier transformed and exploited to generate two-dimensional frequency domain exchange spectra. Directly in the time domain, a variation of the mixing time t_m has variously been used for an efficient access to ultraslow motional time scales [23, 29, 37, 38, 41]. By exploiting the long-time ($t_m \rightarrow \infty$) limit of the F_2 correlation functions, typically designated as final-state amplitude [41]

---

[2] In Ref. [23] examples for frequency distributions were given for $N=2$ sites. For $N \geq 3$ sites the analytical expressions are even more complex so that we refrain from reproducing them here.

[3] The situation in which the central-transition frequency ω_c involves also CS contributions was discussed in Ref. [28].

$$Z^{\cos,\sin}(t_{\mathrm{p}}) = \frac{\left\langle F_2^{\cos,\sin}(t_{\mathrm{p}}, t_m \to \infty, t_{\mathrm{p}}) \right\rangle}{\left\langle F_2^{\cos,\sin}(t_{\mathrm{p}}, t_m \to 0, t_{\mathrm{p}}) \right\rangle}, \tag{26}$$

detailed information concerning the geometry of molecular motion can be inferred if the evolution time t_{p} is varied. In the general case Eq. (26), where the acute brackets indicate a powder average, has to be evaluated numerically. However, in the limit $t_{\mathrm{p}} \to 0$, based on the frequency distribution given in Eq. (24), analytical expressions can be derived for the final-state amplitude

$$Z_{t_{\mathrm{p}} \to 0}(\varphi, \eta) = \frac{\left\langle \overline{\omega_{c,N}^2}(\theta, \phi, \varphi, \eta) \right\rangle}{\left\langle \omega^2(\theta, \phi) \right\rangle}. \tag{27}$$

Here, $\left\langle \overline{\omega_{c,N}^2}(\theta, \phi, \varphi, \eta) \right\rangle$ is the *non-central* second moment (calculated with respect to the angles θ and ϕ) of the distribution of *averaged* frequencies and $\left\langle \omega^2(\theta, \phi) \right\rangle$ is the *non-central* second moment of the single-pulse absorption spectrum). Since Eq. (24) does not change for $N \geq 5$ sites, the same holds for final-state amplitudes based on the second-order quadrupolar anisotropy.

Conversely, for first-order couplings, fast-motion spectra and final-state amplitudes cease to change for $N \geq 3$ equally populated sites. This is because first-order couplings relate to cubic (or octahedral) symmetry, while second-order couplings refer to icosahedral symmetry [42]. For $N \geq 3$ equivalent sites and $\eta \neq 0$, the final-state amplitudes relating to first-order interactions we find

$$\tilde{Z}_{t_{\mathrm{p}} \to 0}^{N \geq 3} = \frac{3[1 + \eta + (3 - \eta) \cos \varphi]^2}{16(\eta^2 + 3)}. \tag{28}$$

In this relation, which was not given before, the ~ sign is meant to emphasize that here we deal with first-order final-state amplitudes. For $\eta = 0$, Eq. (28) reduces to an expression agreeing with that in Ref. [43]. Final-state amplitudes resulting under MAS conditions are briefly discussed in the Supplementary Material.

2.4 Decomposing 2D Spectra for N-Site Cone Models

In this subsection, we will show that two-dimensional (2D) exchange spectra for *N*-site cone models can be built up from a (weighted) superposition of spectra relating to suitably defined two-site jumps. While the idea to decompose 2D exchange patterns into subspectra has been used before [4, 30], we are not aware that the parameters of the corresponding two-site jumps were given previously.

The *s*-th of the *N* sites (on the red cone in Fig. 2) is generated by an Euler rotation about $\Omega_2^{(s)} = (\alpha, \beta, 2\pi s/N)$, cf. Fig. 1. With the Euler rotation $\Omega_{\Delta s}$ from site *r* to site *s* so that $\Delta s = |r - s|$, and with $S_{N=2}(\omega_1, \omega_2; \Omega_{\Delta s})$ designating a two-site 2D subspectrum, the exchange contribution to the full *N*-site 2D spectrum can be written as
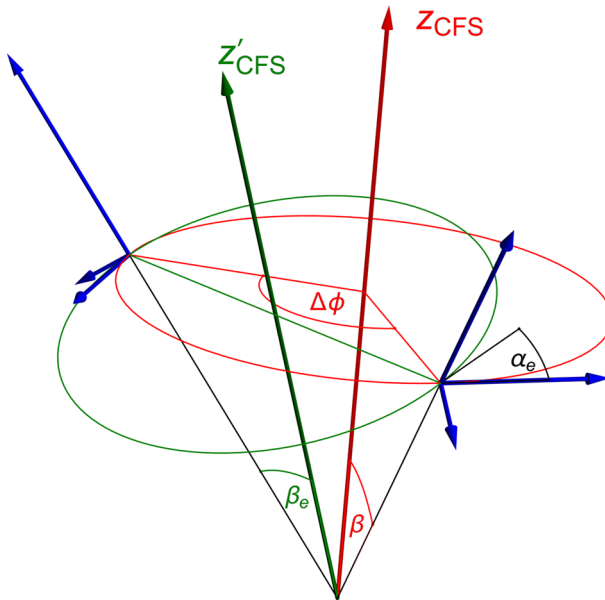
Fig. 2 Two sites of an N-site cone model as represented by the semi-axes of their EFG tensors. The corresponding (original) cone with its half opening angle β is represented by its symmetry axis (z_{CFS}) and a disk, both colored in red. The semi-axes of the tensors are represented in blue: the largest ones are oriented along the mantle of this cone and the second-largest tangential to the circumference of the (red) disk. The two sites are part and on opposite sides of a second cone with half opening angle β_e (and with symmetry axis and disk represented in green). The disks relating to the two cones (or likewise the symmetry axes z_{CFS} and z'_{CFS}) enclose an angle α_e (color figure online)

$$S_N(\omega_1, \omega_2) = \sum_{\Delta s = 1}^{\text{int}(N/2)} W_{\Delta s} S_{N=2}(\omega_1, \omega_2; \Omega_{\Delta s}). \tag{29}$$

Here, a weighting factor $W_{\Delta s}$ is introduced. For odd N, it is given by $W_{\Delta s} = N$ with $\Delta s \leq (N-1)/2$; with even N it is $W_{\Delta s} = N$ for $\Delta s \leq N/2 - 1$ and $W_{\Delta s} = N/2$ for $\Delta s = N/2$. The overall amplitude of the superposed spectrum can be normalized if needed.

The two-site subspectra $S_{N=2}(\omega_1, \omega_2; \Omega_{\Delta s})$ refer to jumps that take place on a cone with an effective half opening angle β_e, cf. Fig. 2, with

$$\beta_e = \frac{1}{2} \arccos\left(1 - 2\sin^2\left(\frac{\pi \Delta s}{N}\right) \sin^2 \beta\right). \tag{30}$$

The Euler angles for the two sites with $s = 0$ and 1 are $\Omega_2^{(0)} = \left(\alpha - \alpha_e, \beta_e, 0 \right)$ and $\Omega_2^{(1)} = \left(\alpha + \alpha_e, \ \beta_e, \pi \right)$ with

$$\alpha_e = \arctan \sqrt{\frac{1 - \sin^2 (\pi \Delta s / N)}{\sin^2 (\pi \Delta s / N) \ \cos^2 \beta}}, \tag{31}$$

so that the rotation between them is described by $\Omega_{\Delta s} = \left(\alpha_e + \alpha, \ 2\beta_e, \pi + \alpha_e - \alpha \right)$.

Thus, by employing the effective angles α_e and β_e, 2D exchange spectra for N-site cone models can easily be obtained for arbitrary N. As an example, as Supplementary Material we show a 2D spectrum generated using the tensor parameters pertaining to the three-site jump in $NaNO_3$ [11], see Fig. S2, which nicely matches with the spectrum published in Ref. [11]. The spectrum shown as Fig. S2 refers to mixing times $t_m \to \infty$. To capture the situation for finite mixing times, it is a simple matter to add the relevant subspectra with the appropriate t_m-dependent weights. The procedures outlined in this section are of course not restricted for application to the central transition or to second-order anisotropies, but can be exploited for any spectra related to N-site jumps, in general.

3 Experimental Details

Solid-state oxygen-17 NMR experiments on $NaNO_3$ were carried out using different spectrometers: A homebuilt spectrometer operated at a Larmor frequency $\omega_L / 2\pi$ of 54.3 MHz was used as well as a Bruker Avance III HD spectrometer operated at 81.4 MHz. For both, the solid-state $\pi/2$ pulse length $t_{\pi/2}$ was about 3.2 μs. The spectrometers were tuned with $H_2^{17}O$ which also served as chemical shift reference. The spectra were obtained using a $\pi/2$-Δ-π sequence employing a pulse spacing Δ that typically was set to 15.2 μs. All spectra were acquired at 81.4 MHz. Stimulated-echo and spin–lattice relaxation experiments were carried out at 54.3 MHz.

Temperature dependent stimulated-echo decay curves were measured using three-pulse sequences. Evolution time dependent stimulated echoes were recorded using a four-pulse sequence to avoid the impact of receiver dead time.

For the preparation of ^{17}O-labeled $NaNO_3$, starting from 40% enriched H_2O (Sigma-Aldrich), we followed the procedures outlined in [11]. The degree of ^{17}O enrichment was determined using high-resolution oxygen-17 NMR and was found to be about 4.5%. To check the crystal structure of the isotope labeled sample, X-ray diffraction was performed. As detailed in the Supplementary Material the rhombohedral structure (space group $R\overline{3}c$, [44, 45]) was nicely confirmed.
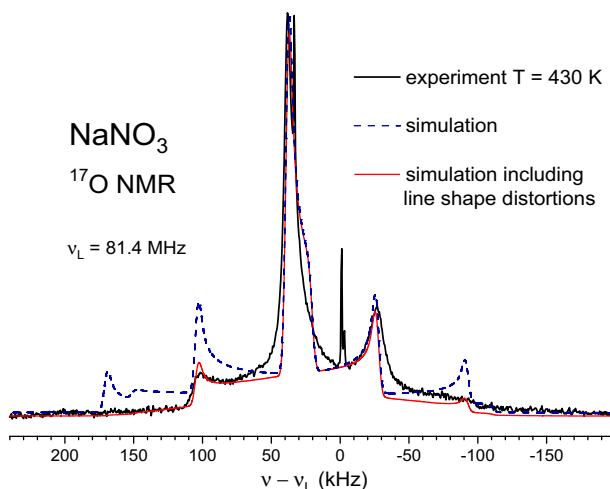
Fig. 3 This high-temperature spectrum (thick black line) of NaNO$_3$ including central- and satellite-transition contributions was acquired by co-adding about 4×10^5 scans. The spectrum is measured using a $\pi/2$-Δ-π echo sequence with a $t_{\pi/2}$ pulse length of 3.2 μs, an interpulse delay of $\Delta = 15.2$ μs, and a repetition time 50 ms. For the experimental spectrum and for the simulated spectrum (dashed blue line), Gaussian apodization with $\sigma = 2\pi \times 200$ Hz was used. Another simulated spectrum (red thin solid line) is shown which is obtained from the other by multiplication with a sinc as well as a Lorentzian function. Impurity related narrow peaks with an integrated intensity of 0.5% and 1.3% of the total appear near 33 kHz (NO$_3$ group) and $-$ 1 kHz (H$_2$O), respectively (color figure online)

4 Results and Analyses

4.1 High-Temperature Spectrum

The NaNO$_3$ spectra should reach their terminally narrowed form when the molecular reorientation rates approach 10^{-10} s. Therefore, we recorded a spectrum at a temperature of 430 K (the highest temperature safely accessible with our probe head) which is somewhat larger than the temperature reached in [11].[4] The experimentally obtained spectrum, shown in Fig. 3, is seen to span a width of about 250 kHz. The spectrum of NaNO$_3$ was excited at a center frequency of 14.8 kHz with respect to the ^{17}O resonance of H$_2$O that served as reference. Owing to a significant (positive) isotropic chemical shift of NaNO$_3$ and a limited effective excitation width of about 78 kHz $\approx 1/(4t_{\pi/2})$, the spectrum appears somewhat skewed and displays larger intensity on its high-frequency side. On this side, not only the inner but also an outer satellite is clearly resolved. We then calculated the full spectrum using the quadrupolar and chemical shift parameters given in [11] which are $C_Q = 12.5$ MHz, $\eta_Q = 0.8$, and $\Omega_{\text{CFS} \rightarrow \text{EFG}} = [0°, 90°, 0°]$ as well as $[\delta_{33}, \delta_{22}, \delta_{11}] = [250, 400, 550]$ ppm and $\Omega_{\text{CFS} \rightarrow \text{CSA}} = [90°, 180°, 0°]$. The latter parameters correspond [53] to an

---

[4] A spectrum that we recorded at 400 K was much less intense and broadened as compared to the spectrum shown in Fig. 3 for 430 K.

isotropic chemical shift $\sigma_{iso} = (\sigma_{33} + \sigma_{22} + \sigma_{11})/3 = 400$ ppm, a shielding anisotropy $\zeta_{CS} = 150$ ppm, and an asymmetry parameter $\eta_{CS} = 1$. The high-temperature spectrum shown in Fig. 3 is in the ultrafast motion regime and hence the fully averaged parameters are $\overline{C}_Q = 1.25$ MHz, cf. Eq. (20). Furthermore, $\overline{\eta}_Q = 0$ and of course σ_{iso} remain unaltered. Then, one has $\overline{\zeta}_{CS} = 150$ ppm (with $N_{CS} = 1$, the sign of $\overline{\zeta}_{CS}$ is indeterminate for $\eta_{CS} = 1$) and $\overline{\eta}_{CS} = 0$. A better fit of the experimental high-temperature spectrum was, however, achieved using $\overline{C}_Q = 875$ kHz. Based on the full $C_Q = 12.5$ MHz, an asymmetry parameter $\eta_Q = 0.86$ (rather than 0.8) would lead to the latter $\overline{C}_Q$.

The positions of all spectral features visible in the experimentally recorded spectrum are clearly also seen in the simulations, see Fig. 3, except for the narrow resonances appearing near 33 kHz ($= 406$ ppm) and -1 kHz ($= -12$ ppm). These two peaks were also observed in [11] and in that work they were assigned to the oxygen resonances of ^{17}O enriched H_2O and dissolved $NaNO_3$, respectively.

To account (at least partially) for the observed skewing and broadening of the spectra that originate from the noncentered radio-frequency excitation, the finite pulse width, the limited spectral band width [46], and possibly from other effects as well, another simulated spectrum is shown in Fig. 3. That spectrum was obtained by multiplying the other simulated spectrum with the product of a Lorentzian and a sinc function. For the Lorentzian broadening, with $[1 + (\nu/\nu_B)^2]^{-1}$, we have chosen $\nu_B = 200$ kHz; for the sinc function, an argument of $2\pi\nu t_{\pi/2}$. The Lorentzian and the sinc function are both centered at the irradiation frequency of 14.8 kHz ($= 181$ ppm). As seen in Fig. 3, this procedure provides a satisfactory description of the experimental spectrum.

Based on the above parameters, the central-transition line width purely originating from the second-order quadrupolar interaction can be assessed via [47]

$$\Delta\nu_{CT}^{(Q)}(C_Q, \eta_Q) = \frac{(2I + 3)[\eta_Q^2 + 22\eta_Q + 25)]}{256I^2(2I - 1)} \frac{C_Q^2}{\nu_L}. \tag{32}$$

Using $\overline{C}_Q = 875$ kHz and $\overline{\eta}_Q = 0$, at 81.4 MHz, this relation gives $\Delta\overline{\nu}_{CT}^{(Q)} = \Delta\nu_{CT}^{(Q)}(\overline{C}_Q, \overline{\eta}_Q) = 294$ Hz. Only considering a chemical shielding anisotropy of $\zeta_{CS} = 150$ ppm (without quadrupolar broadening) results in a much larger width of about $\frac{3}{2}\nu_L\zeta_{CS} \approx 18.3$ kHz. Although the contributions stemming from the two different interactions are not simply additive, it is clear that the high-temperature central-transition absorption line is by far dominated by chemical shielding effects. To render the small width $\Delta\overline{\nu}_{CT}^{(Q)}$ visible, it is necessary to perform high-temperature MAS experiments. However, with our MAS probe head only temperatures up to 400 K could be reached. A spectrum recorded at that temperature while spinning the sample with 20 kHz unfortunately did not exhibit the required resolution.

A reliable detection of the residual quadrupolar-induced shift is also not straightforward. According to Eq. (22), the expected residual shift is $\overline{\nu}_{CG}^{(Q)} = -56$ Hz ($= -0.7$ ppm, calculated using $\overline{C}_Q = 875$ kHz and $\overline{\eta}_Q = 0$). For

Fig. 4 Solid lines represent experimentally determined central-transition ^{17}O NMR spectra of $NaNO_3$ recorded at a field of 14.1 T for a range of temperatures. The spectra were measured using a $\pi/2$-Δ-π echo sequence with an interpulse delay of $\Delta = 15.2$ μs and repetition times of 10 s for 158 K and 167 K, 5 s for 176 K, 2 s for 186 K, 0.2 s for 194 K, and 0.1 s for 204 to 241 K. The dashed lines represent results obtained from random walk simulations: By adjusting the motional correlation times τ of the nitrate moiety used in the simulations to the values given in the figure, an acceptable match of experimental and numerically simulated spectra is achieved. For the experimental and the simulated spectra, Gaussian apodization with $\sigma = 2\pi \times 1$ kHz was used
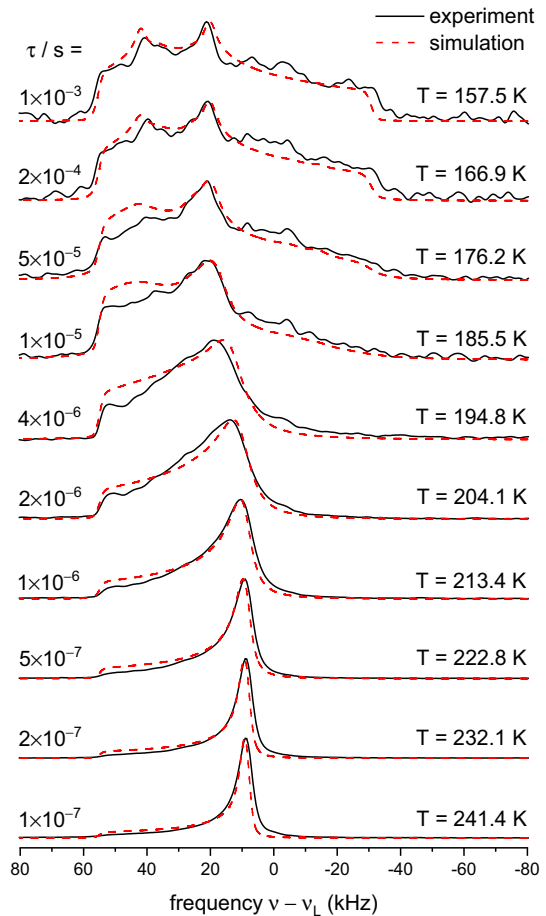
Fig. 5 Stimulated ^{17}O sin–sin echo decay curves measured for $NaNO_3$ at a field of 9.4 T for an evolution time $t_p = 20$ μs. The solid lines reflect fits using Eq. (33). Corresponding cos-cos curves are presented as Supplementary Material
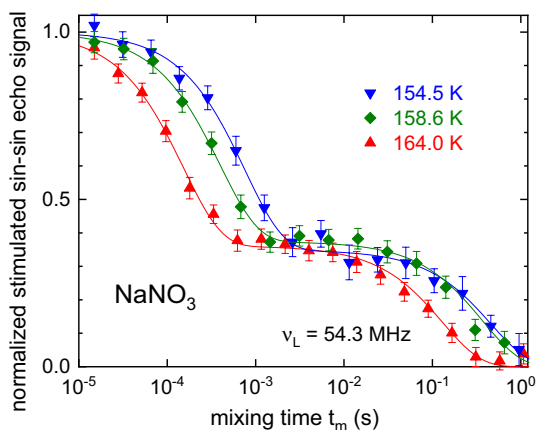
Fig. 6 Final-state amplitudes $Z^{cos}(t_p)$ and $Z^{sin}(t_p)$, represented as circles and squares, respectively, as measured for NaNO$_3$ at 160 K using ^{17}O NMR. Numerical calculations, based on Eq. (26) and represented as solid lines, are seen to provide a useful description of the experimental data. The experimental evolution times t_p were right shifted by $t_{\pi/2} = 3.25$ μs to account for effects of finite pulse lengths
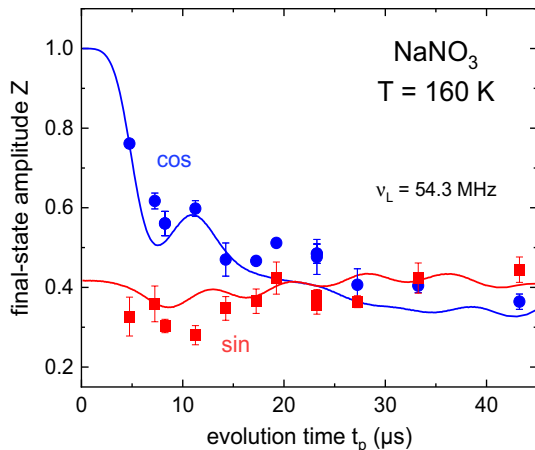
comparison, based on the low-temperature parameters $C_Q = 12.5$ MHz and $\eta_Q = 0.8$, one has $v_{CG}^{(Q)} = -14.0$ kHz ($=-171$ ppm). Using $\bar{v}_{iso}^{(CS)}$ ($= 32.6$ kHz at $\nu_L = 81.4$ MHz), one may thus assess $\bar{v}_{CG}^{exp} = v_{iso}^{(CS)} + \bar{v}_{CG}^{(Q)}$.

4.2 Low-Temperature Spectra

When lowering the temperature to below 430 K, the intensity of the central and sat-ellite transitions becomes faint and down to about room temperature in fact only the residual resonances from traces of H$_2$O and dissolved NaNO$_3$ appear with sig-nificant intensity. Consistent with previous data [11], at a field of 14.1 T significant central intensity does reappear only below 280 K. Then, more or less symmetric central-transition spectra are observed which eventually develop a more asymmetric shape somewhat below ≈ 250 K, see Ref. [11] as well as Fig. 4.

Upon lowering the temperature further, a central-transition pattern evolves that overall is about 100 kHz broad. Using random walk simulations of the type detailed in Ref. [23] and employing the published tensor parameters [11], we obtained the spectra shown as dashed lines in Fig. 4. For the simulations, the reorientation rate describing the threefold motion of the NO$_3^-$ group was adjusted until a satisfactory match of calculations and experimental data was found. The resulting, temperature dependent correlation times are discussed below, in Sect. 5.

4.3 Stimulated-Echo Spectroscopy

Stimulated-echo decay functions, cf. Eq. (25), when measured as a function of mix-ing time t_m and evolution time t_p yield direct insights into time scale and geometry of the molecular motion. In Fig. 5, we show F_2 curves recorded at a fixed $t_p = 20$ μs for several temperatures. For all curves, one recognizes a clear two-step decay. The first of these is due to a decorrelation of the molecular orientations and the one
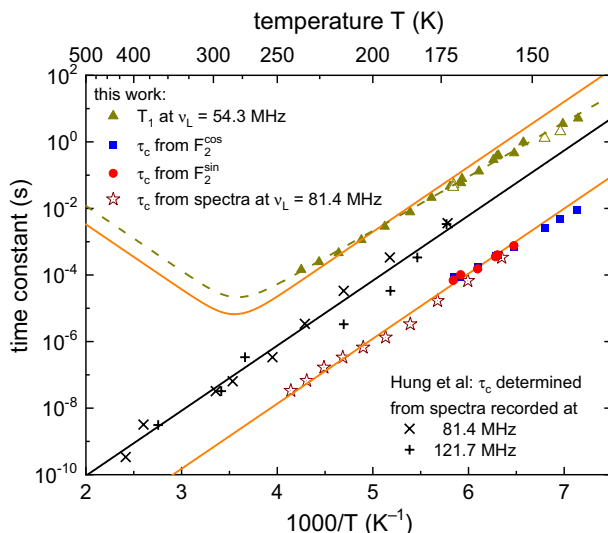
Fig. 7 Arrhenius diagram summarizing variously determined correlation times relating to the threefold nitrate ion motion in $NaNO_3$. All data are from the present work except the correlation times represented by plusses and crosses that are from [11]. These latter data, given here as $\tau = (3 \, k)^{-1}$, are based on analyses of line shapes measured at 21.1 and 14.1 T, respectively. The straight solid lines reflect Arrhenius laws with an activation energy of 37 kJ mol^{-1}. The solid curve refers to spin–lattice relaxation times calculated using Eq. (35) for a BPP spectral density at $\omega_L = 2\pi \times 54.3$ MHz with the parameters $\tilde{C}_Q = C_Q = 12.5$ MHz, $\eta_Q = 0.8$, $\tau_0 = 2.1 \times 10^{-16}$ s, and $E = 37$ kJ mol^{-1}. Experimentally determined spin–lattice relaxation times are represented as closed triangles (those from the final decay of the stimulated-echo signals as open triangles). The dashed curve represents a Cole-Davidson fit using Eq. (35) with $\gamma_{CD} = 0.85$, $\tilde{C}_Q = 0.58 C_Q$, $\eta_Q = 0.8$, $\tau_0 = 2.1 \times 10^{-16}$ s, and $E = 37$ kJ mol^{-1}

appearing at longer times reflects spin–lattice relaxation, i.e., a decay of the longitudinal magnetization that can be parameterized using $M(t) \propto \exp(-t_m/T_1)$. Here, T_1 designates the spin–lattice relaxation time.

For a quantitative assessment of the data shown in Fig. 5, we have chosen the function

$$S_2(t_p, t_m) \propto [(1 - Z)\exp(-t_m/\tau) + Z]M_2(t_m). \tag{33}$$

which describes our data well. Important fit parameters are the correlation time τ (which will be discussed in Sect. 5, below) as well as the final-state amplitude $Z(t_p)$, cf. Eq. (26). For a given evolution time, Z is expected to be temperature independent if the geometry of the molecular motion remains unchanged. Figure 5 shows that, within experimental uncertainty, this is indeed the case.

Measurements of this type were also performed as a function of the evolution time t_p at a temperature of 160 K. The resulting correlation times were found to be independent of the evolution time. In Fig. 6, we show the final-state amplitudes $Z(t_p)$ obtained from these measurements.

Using the procedures outlined in Sect. 2.3 and the published [11] tensor parameters, we computed the final-state amplitudes employing Eq. (26). In Fig. 6, one recognizes that this approach describes the measured Z values very well.

5 Discussion

The time scales determined using the present line shape analyses (cf. Fig. 4) and the decay times assessed from the stimulated-echo functions (cf. Fig. 5) are compiled in Fig. 7. The exchange rates k obtained from previous line shape analyses [11] are also included in this figure. Note that if k designates the rate constant for a jump between two sites, then for a three-site jump, k corresponds to a correlation time $\tau = (3k)^{-1}$ [48]. The temperature dependence of all these time scales conforms to the previously reported thermally activated behavior with an activation energy $E = 37$ kJ mol^{-1} [11]. In other words, the correlation times obey an Arrhenius law

$$\tau = \tau_0 \exp(E/k_B T), \tag{34}$$

where τ_0 designates an inverse attempt frequency. Following [11], the rate k_0 is given as e^{31} s$^{-1} = 2.9 \times 10^{13}$ s^{-1}. The corresponding inverse attempt frequency thus is $(3k_0)^{-1} = 1.1 \times 10^{-14}$ s, while the data from the present work yield $\tau_0 = 2.1 \times 10^{-16}$ s. Currently, we are unable to rationalize the discrepancy of these values.

Correlation times τ can be estimated also from measurements of spin–lattice relaxation times T_1, e.g., from data such as those shown in Fig. 5 for long mixing times. The corresponding T_1 times as well as those measured independently at a Larmor frequency of 54.3 MHz using saturation recovery ($T \leq 150$ K) and inversion recovery ($T > 150$ K) sequences are also included in Fig. 7; we have not been able to record spin–lattice relaxation times for temperatures above 250 K.

From Fig. 7 one recognizes that the temperature dependence of the available spin–lattice relaxation times is somewhat less pronounced than that from the other quantities. In the simplest case, correlation times τ can be estimated from T_1 experiments by virtue of [49]

$$\frac{1}{T_1^{(Q)}} = \frac{3(2I+3)}{200I^2(2I-1)} \left(2\pi \tilde{C}_Q\right)^2 \left(1 + \tfrac{1}{3}\eta_Q^2\right) \left[J(\omega_L) + 4J(2\omega_L)\right], \tag{35}$$

where the spectral density has the form $J_{BPP}(\omega_L) = \tau/[1 + (\omega_L \tau)^2]$. This expression is due to Bloembergen, Purcell, and Pound (BPP) and refers to the presence of a single correlation time. Furthermore, the expression for $1/T_1^{(Q)}$ assumes the prevalence of a (first-order) quadrupolar relaxation mechanism and $\tilde{C}_Q$ (in Hertz) denotes the fluctuating part of the quadrupolar coupling constant. In Eq. (35), the I-dependent prefactor is 3/625 for $I = 5/2$.

Based on the presently determined τ_0 and for simplicity identifying $\tilde{C}_Q$ with C_Q, the T_1 contribution relating to the correlation times measured in this work was calculated using Eq. (35) with the existence of a BPP spectral density

assumed. The thus calculated temperature dependence for T_1, see the solid curve in Fig. 7, is somewhat steeper than indicated by the measured spin–lattice relaxation times, suggesting that a distribution of correlation times might be present. To test this conjecture, we have chosen the distribution invented by Cole and Davidson (CD) [50] which leads to a spectral density of the form [51]

$$J_{CD}(\omega_L) = \omega_L^{-1}(1 + \omega_L^2\tau^2)^{-\gamma_{CD}/2} \sin[\gamma_{CD} \arctan(\omega_L\tau)]. \tag{36}$$

Here, γ_{CD} characterizes the distribution width ($0 < \gamma_{CD} \leq 1$) and the non-distributed case corresponds to $\gamma_{CD} = 1$. Calculations using this approach agree very well with the experimental data for a width parameter $\gamma_{CD} = 0.85$ if, for the fluctuating part of the coupling constant, a reduced value of $\tilde{C}_Q = 0.58 C_Q$ is considered. Such a reduction is consistent with the presence of an anisotropic motion of the oxygen EFG tensors which does not modulate the quadrupolar frequencies in full. In particular towards higher temperatures, when approaching the structural $R\bar{3}c \rightarrow R\bar{3}m$ phase transition of $NaNO_3$ that takes place at 553 K, effects of positional disorder of the NO_3 group [45] may additionally affect these tensors.

The agreement of the CD fit with the experimental spin–lattice relaxation times, seen in Fig. 7, confirms that the spin–lattice relaxation is dominated by the threefold motion of the NO_3 group. Hence, rather than using an exponential function in Eq. (33), a form for the correlation function should have been chosen for the data in Fig. 5 that reflects a (narrow) distribution of time constants. Since time correlation functions corresponding to the Cole–Davidson form are somewhat complicated, we have chosen the practically equivalent stretched exponential Kohlrausch–Williams–Watts form, $\exp[-(t_m/\tau)^{\beta_K}]$. The width parameter $\gamma_{CD} = 0.85$ relates [52] to a Kohlrausch exponent $\beta_K \approx 0.9$.[5] As demonstrated in the Supplementary Material, fits using this exponent describe the F_2 data equally well.

6 Concluding Remarks

In the present work, one focus has been on second-order quadrupolar effects that persist up to the regime of extreme narrowing in samples featuring *anisotropic* internal motions. By averaging over the sites accessible in the course of the molecular jump process prior to applying the secular approximation, we obtain the averaged quadrupolar coupling $\overline{C}_Q$ and the averaged asymmetry parameter $\overline{\eta}_Q$, thus recovering results analogous to those known in the context of first-order anisotropies. Furthermore, we calculated the residual quadrupolar-induced shift which in the regime of extreme narrowing can be expressed in terms of $\overline{C}_Q$ and $\overline{\eta}_Q$. Specifically, we applied these results to *N*-site cone models. An interesting finding is that in the regime of terminal motional narrowing the quadrupolar spectra do not change for $N \geq 3$. Conversely, in the regime of what we call intermediate narrowing this happens only for

---

[5] Following Ref. [52] the Kohlrausch exponent β_K is related to the width parameter γ_{CD} according to $\beta_K = 0.683_{CD} + 0.316$ for $0.6 \leq \gamma_{CD} \leq 1.0$. For $\gamma_{CD} = 0.85$ this relation yields $\beta_K \approx 0.9$.

$N \geq 5$, a result that can be traced back to the icosahedral symmetry of the second-order quadrupolar interaction.

While the above results refer to fast and ultrafast motions, we also considered the regime of slow and ultraslow motions where 2D experiments can be carried out in the frequency as well as in the time domains. Referring to N-site jumps, for the latter in the limit of vanishing evolution times we calculated the final-state amplitudes accessible using stimulated echoes analytically. Again for $N \geq 5$ sites, we find that these amplitudes cease to change. Furthermore, we have shown how two-dimensional spectra can be decomposed in terms of effective two-site jumps. This decomposition is applicable not only for the considered cone models, but in fact also for numerous other models. The limit of mixing times $t_{\mathrm{m}} \rightarrow \infty$ was considered explicitly, with the generalization to finite mixing times being a simple matter. We tested this approach successfully for the three-site jump of the planar NO_3 group in $NaNO_3$ by comparing the results of the decomposition procedure with conventional simulations: Both agree with each other and with a previously determined experimental spectrum [11].

In the experimental part of the present work, we studied $NaNO_3$ which was previously examined via ^{17}O NMR mostly using line shape analyses [11]. Additionally, we employed central-transition stimulated-echo spectroscopy, extending the previously accessible dynamic range to slightly longer times, thereby confirming the reported activation energy. For reasons which are unclear at present, however, at any given temperature, we find considerably shorter correlation times than those inferred from [11]. From the correlation times determined in the present study, spin-relaxation times were calculated and good agreement with the experimental results was achieved.

The evolution time-dependent final-state amplitudes measured at low temperatures agree well with our theoretical predictions. At high temperatures, i.e., in the regime of extreme narrowing, we were able to record a "full" [17]O spectrum including the central as well as the satellite transitions in nonrotating $NaNO_3$. It turns out that the shape of the central transition is dominated by anisotropic chemical shift rather than by quadrupolar effects. Hence, for a sensitive laboratory test of some of the theoretical calculations advanced in the present work, either high-temperature MAS experiments should be carried out. Alternatively, oxygen-17 studies for liquids or crystals featuring, e.g., SO_3 or NO_2 groups in which the oxygen EFG tensors perform (fast) nonplanar motions will be beneficial in this respect.

7 Supplementary Material

In the Supplementary Material, we present (1) calculations of final-state amplitudes for N-site cone models with $N \geq 3$ equivalent sites referring to stationary samples and for $N \geq 2$ sites referring to samples subjected to fast MAS, (2) a simulated 2D

spectrum obtained by the procedures outlined in Sect. 2.4, (3) results from powder X-ray diffraction of an ^{17}O-labeled NaNO$_3$ crystal, and (4) cos–cos decay curves.

Appendix

For the chemical shift, the Hamiltonian can be written as [32]

$$H_{\text{CS,LAB}} = \omega_L \sigma_{\text{iso}} T_{1,0} + \sum_{l=1,2} \sum_{m=-l}^{l} (-1)^m V_{l,-m}^{\text{CS,LAB}} T_{l,m}, \qquad (37)$$

where $\sigma_{\text{iso}} = \frac{1}{3}(\sigma_{XX} + \sigma_{YY} + \sigma_{ZZ})$ denotes the isotropic chemical shielding. Note that according to Eq. (3) a sequence of three transformations is now required if one starts from the PAS components which involve the shielding anisotropy $\zeta_{\text{CS}} = \sigma_{ZZ} - \sigma_{\text{iso}}$, and the shielding asymmetry $\eta_{\text{CS}} = (\sigma_{YY} - \sigma_{XX})/(\sigma_{ZZ} - \sigma_{\text{iso}})$. Regarding the definition of the latter quantities and the ordering $|\sigma_{ZZ} - \sigma_{\text{iso}}| \geq |\sigma_{XX} - \sigma_{\text{iso}}| \geq |\sigma_{YY} - \sigma_{\text{iso}}|$ we follow the Haeberlen notation [53]. For $l=2$ the CS tensor components are [54]

$$V_{2,0}^{\text{CS,PAS}} = \sqrt{\frac{3}{2}} \omega_{\text{L}} \zeta_{\text{CS}}, \quad V_{2,\pm1}^{\text{CS,PAS}} = 0, \quad V_{2,\pm2}^{\text{CS,PAS}} = \frac{1}{2} \eta_{\text{CS}} \omega_{\text{L}} \zeta_{\text{CS}}. \qquad (38)$$

Cross terms among the quadrupolar and chemical shift interaction, involving the $l=1$ terms in Eq. (37), are typically 10^6 times smaller than the quadrupolar coupling [54]. Albeit small, corresponding phenomena were observed using satellite-transition MAS spectroscopy [54]. However, in the present context such effects need not be considered.

Applying the secular approximation to the chemical shift Hamiltonian one obtains [54]

$$\bar{H}_{\text{CS}}^{(1)} = \omega_{\text{L}} \sigma_{\text{iso}} I_z + \sqrt{\frac{2}{3}} \bar{V}_{2,0}^{\text{CS,LAB}} I_z. \qquad (39)$$

Since *second-order* chemical shift effects are irrelevant, analogous to the arguments made near Eq. (13), there are no line shape changes relating to the chemical shielding when going from the fast-motion to the extreme-narrowing regime.

References

1. J.S. Waugh, E.I. Fedin, Phys. Solid State **4**, 1633 (1963)
2. V. Macho, L. Brombacher, H.W. Spiess, Appl. Magn. Reson. **20**, 405–432 (2001)
3. M.R. Hansen, R. Graf, H.W. Spiess, Acc. Chem. Res. **46**, 1996–2007 (2013)
4. K. Schmidt-Rohr, H.W. Spiess, *Multidimensional Solid-State NMR and Polymers* (Academic Press, London, 1994)
5. G. Wu, Prog. Nucl. Magn. Reson. Spectrosc. **114**, 135–191 (2019)
6. S. Sen, Prog. Nucl. Magn. Reson. Spectrosc. **116**, 155–176 (2020)
7. R.E. Wasylishen, S.E. Ashbrook, S. Wimperis (eds.), *NMR of Quadrupolar Nuclei in Solid Materials* (Wiley, Chichester, 2012)
8. M. Witschas, H. Eckert, H. Freiheit, A. Putnis, G. Korus, M. Jansen, J. Phys. Chem. A **105**, 6808–6816 (2001)
9. M. Duer, *Introduction to Solid State NMR Spectroscopy* (Blackwell Publishing Ltd., Oxford, 2004)
10. R.W. Schurko, S. Wi, L. Frydman, J. Phys. Chem. A **106**, 51 (2002)
11. I. Hung, G. Wu, Z. Gan, Solid State Nucl. Magn. Reson. **84**, 14–19 (2017)
12. F.H. Larsen, J. Magn. Reson. **171**, 293–304 (2004)
13. R.L. Vold, G.L. Hoatson, J. Magn. Reson. **198**, 57 (2009)
14. S.H. Chung, K.R. Jeffrey, J.R. Stevens, J. Chem. Phys. **108**, 3360 (1998)
15. M. Witschas, H. Eckert, J. Phys. Chem. A **103**, 10764 (1999)
16. J. Shen, V. Terskikh, G. Wu, ChemPhysChem **20**, 268–275 (2019)
17. A. Baram, Z. Luz, S. Alexander, J. Chem. Phys. **58**, 4558 (1973)
18. L. Werbelow, J. Chem. Phys. **104**, 3457 (1996)
19. J. Zhu, E. Ye, V. Terskikh, G. Wu, J. Phys. Chem. Lett. **2**, 1020–1023 (2011)
20. J. Beerwerth, S.P. Bierwirth, J. Adam, C. Gainaru, R. Böhmer, J. Chem. Phys. **150**, 194503 (2019)
21. L. Hoffmann, J. Beerwerth, D. Greim, J. Senker, C. Sternemann, W. Hiller, R. Böhmer, J. Chem. Phys. **152**, 034503 (2020)
22. Y. Dai, I. Hung, Z. Gan, G. Wu, Concepts Magn. Reson. **45A**, e21409 (2016)
23. J. Beerwerth, M. Storek, D. Greim, J. Lueg, R. Siegel, B. Cetinkaya, W. Hiller, H. Zimmermann, J. Senker, R. Böhmer, J. Magn. Reson. **288**, 84–94 (2018)
24. J. Lu, I. Hung, A. Brinkmann, Z. Gan, X. Kong, G. Wu, Angew. Chem. Int. Ed. **56**, 6166–6170 (2017)
25. X. Kong, L.A. Dell, V. Terskikh, E. Ye, R. Wang, G. Wu, J. Am. Chem. Soc. **134**, 14609–14617 (2012)
26. M.T. Dunstan, J.M. Griffin, F. Blanc, M. Leskes, C.P. Grey, J. Phys. Chem. C **119**, 24255–24264 (2015)
27. M. Nava, N. Lopez, P. Müller, G. Wu, D.G. Nocera, C.C. Cummins, J. Am. Chem. Soc. **137**, 14562–14565 (2015)
28. W.D. Wang, B.E.G. Lucier, V.V. Terskikh, W. Wang, Y.N. Huang, J. Phys. Chem. Lett. **5**, 3360–3365 (2014)
29. M. Adjei-Acheamfour, J. Tilly, J. Beerwerth, R. Böhmer, J. Chem. Phys. **143**, 214201 (2015)
30. S. Wefing, H.W. Spiess, J. Chem. Phys. **89**, 1219 (1988)
31. A. Abragam, *The Principles of Nuclear Magnetism* (Oxford University Press, Oxford, 1999)
32. D. Freude, in *Solid-State NMR. Encyclopedia of Analytical Chemistry*, ed. by R.A. Meyers (Wiley, Chichester, 2000), pp. 12188–12224
33. R. Hajjar, Y. Millot, P.P. Man, Prog. Nucl. Magn. Reson. Spectrosc. **57**, 306–342 (2010)
34. M.E. Rose, *Elementary Theory of Angular Momentum* (Dover Publications, New York, 1957)
35. A. Samoson, Chem. Phys. Lett. **119**, 29 (1985)
36. P.P. Man, in *Encyclopedia of Magnetic Resonance*, ed. by R.K. Harris, R.E. Wasylishen (Wiley, Chichester, 2011). https://doi.org/10.1002/9780470034590.emrstm0429.pub2
37. G. Hinze, Phys. Rev. E **57**, 2010 (1998)
38. R. Böhmer, G. Diezemann, G. Hinze, E. Rössler, Prog. Nucl. Magn. Reson. Spectrosc. **39**, 191 (2001)
39. A. Samoson, B.Q. Sun, A. Pines, in *Motional Averaging. Pulsed Magnetic Resonance: NMR, ESR, and Optics: A Recognition of E. L. Hahn*, ed. by D.M.S. Bagguley (Clarendon Press, Oxford, 1992), pp. 80–94
40. M. Adjei-Acheamfour, R. Böhmer, J. Magn. Reson. **249**, 141 (2014)

41. G. Fleischer, F. Fujara, NMR as a Generalized Incoherent Scattering Experiment, in *NMR—Basic Principles and Progress* vol. 30, ed. by P. Diehl, E. Fluck, H. Günther, R.Kosfeld, J. Seelig (Springer, Berlin, 1994), pp. 160–207
42. B.Q. Sun, J.H. Baltisberger, Y. Wu, A. Samoson, A. Pines, Solid State Nucl. Magn. Reson. **1**, 261 (1992)
43. F. Fujara, S. Wefing, H.W. Spiess, J. Chem. Phys. **84**, 4579 (1986)
44. G. Gonschorek, H. Weitzel, G. Miehe, H. Fuess, W.W. Schmahl, Z. Krist. **215**, 752–756 (2000)
45. P. Ballirano, Phys. Chem. Miner. **38**, 531–541 (2011)
46. P.B. Groszewicz, H. Breitzke, G. Buntkowsky, Solid State Nucl. Magn. Reson. **84**, 227–233 (2017)
47. K. MacKenzie, M. Smith, *Multinuclear Solid-State Nuclear Magnetic Resonance of Inorganic Materials* (Pergamon, Amsterdam, 2002)
48. G. Williams, Chem. Soc. Rev. **1**, 89–131 (1978)
49. H.W. Spiess, in *Dynamic NMR Spectroscopy*, vol. 15, ed. by P. Diehl, E. Fluck, R. Kosfeld (Springer, Berlin, 1978), pp. 55–214
50. D.W. Davidson, R.H. Cole, J. Chem. Phys. **19**, 1484 (1951)
51. P.A. Beckmann, Phys. Rep. **171**, 85 (1988)
52. C.P. Lindsey, G.D. Patterson, J. Chem. Phys. **73**, 3348 (1980)
53. R.K. Harris, E.D. Becker, S.M.C. De Menezes, P. Granger, R.E. Hoffman, K.W. Zilm, Pure Appl. Chem. **80**, 59–84 (2008). https://doi.org/10.1351/pac200880010059
54. S. Wi, S.E. Ashbrook, S. Wimperis, L. Frydman, J. Chem. Phys. **118**, 3131 (2003)